

# A New Accelerated Method to Characterize Degradation of Thermal Interface Materials

Pranay P. Nagrani\* and Amy M. Marconnet\*

School of Mechanical Engineering, Purdue University, West Lafayette, IN 47906, USA

E-mail: pnagrani@purdue.edu; marconnet@purdue.edu

#### Abstract

Due to advances in 3D integration and miniaturization of chips, the power density and number of hotspots within electronic packages have increased rapidly. A major bottleneck in the chip-to-coolant thermal resistance pathway is the interfacial resistance at solid-solid contacts and, therefore, thermal interface materials (TIMs) are employed to minimize interfacial thermal resistance. However, thermal greases (paste-like materials) often degrade over time via pumpout (material moves out of the interface) and dryout (phase separation of the composite material) phenomena due to repeated heating and cooling. Traditional reliability testing methods such as thermal cycling have long testing periods. In this study, to accelerate the observation of the degradation of thermal greases, we propose adding mechanical cycling while maintaining a constant heat flow rate. We investigate the reliability of three thermal greases at different oscillation amplitudes and squeezing pressures using a novel custom designed and machined experimental rig. We leverage high-resolution infrared imaging of thermal grease to capture steady-state 2D temperature maps, from which we calculate mechanical and thermal reliability metrics such as void fraction and comparison of area-normalized thermal resistance at the beginning- and end-of-life. Our results uncover that the mechanical reliability of thermal greases depends on the ratio of elastic modulus to viscosity, with higher ratios being more desirable. Meanwhile, the thermal reliability depends upon the synergy of material properties with higher elastic modulus and higher thermal conductivity resulting in a lesser increase in thermal resistance over the lifetime of thermal greases.

Keywords: Thermal Grease, Pumpout, Accelerate Degradation, Mechanical Cycling, Infrared Imaging

### Introduction

With transistors scaled down to a few nanometers, the demand for increasing computational power is now realized by advanced packaging techniques such as the heterogeneous or 3D integration of chiplets. <sup>1,2</sup> However, miniaturization <sup>3–5</sup> combined with 3D integration results in high and non-uniform heat fluxes that necessitate efficient thermal management solutions, often involving single-phase and two-phase liquid cooling. <sup>6,7</sup> Both integration of components within advanced packages and the integration of devices with cold plates or heat sinks results in numerous solid-solid interfaces (e.g., interfaces between dies, between dies and the lid or heat spreader, and between the lid/heat spreader and heat sinks or cold plates). Often the interface thermal resistance is the bottleneck in the overall junction-to-ambient thermal resistance. <sup>8</sup> Thermal interface materials (TIMs) are widely used at the solid-solid interfaces to reduce the interfacial resistance. <sup>9–11</sup> Thermal greases are a common TIM that generally include high thermal conductivity filler particles within a polymer matrix. They reduce the interface thermal resistance due to the relatively high thermal conductivity and conformability of the grease to surface asperities to eliminate air gaps.

Previous studies <sup>12–17</sup> on thermal greases have generally focused on modifying the material properties (such as thermal conductivity, elastic modulus, and yield stress) only at the beginning-of-life (BOL) or *before* deploying such materials at the solid-solid interface. Specifically, many studies focus on reducing the overall interface thermal resistance by enhancing the thermal conductivity, reducing the bondline thickness (BLT, defined as the

interface thickness), and reducing the contact resistances between the thermal grease and the mating surfaces. <sup>10,18–21</sup> However, repeated power cycling of electronic devices results in uneven expansion and contraction of the components between which the thermal grease is sandwiched, due to differences in the coefficient of thermal expansion (CTE) of the different components. This results in the degradation of the thermal grease and, hence, increasing thermal interface resistances with cycling. <sup>22–24</sup> Common modes of degradation are pumpout (movement of TIM out of the interface) and dryout (phase separation of particles and polymer). Therefore, understanding and mitigating such degradation modes is an active area of research to ensure the reliability of electronic packages. <sup>25</sup>

To address this challenge, various approaches have been developed to study the reliability and degradation modes of thermal greases including power cycling, temperature cycling, and relative-humidity tests. <sup>25</sup> To induce degradation, a typical approach is temperature cycling, where a three-layer stack, comprising of the TIM sandwiched between two metallic coupons, is alternatingly cooled and heated within ovens (between -40 °C to 125 °C) for hundreds of cycles. <sup>26–28</sup> After cycling, degradation can then be quantified using tools like scanning acoustic microscopy (SAM) to image voids and pumpout within thermal greases and the reference bar approach to quantify the thermal resistances. However, such reliability studies usually analyze the thermal grease degradation after the testing is completed. To understand the evolution of thermal grease degradation with power cycling in situ, our team<sup>29,30</sup> has studied degradation within commercial thermal greases at different BLTs and cycling frequencies by leveraging thermal imaging and visual imaging. The thermal tests in Nagrani et al. 29 were complemented with rheology tests to highlight the importance of temperature-dependent viscosity hysteresis on thermal grease degradation (as opposed to considering only the single viscosity value typically provided within technical datasheets). Further, Kulkarni et al. 30 conducted statistical analysis to understand the sensitivity of various parameters on thermal grease degradation. One major drawback of such studies is that reliability tests span several days to observe degradation, and high-end thermal greases usually require a much

longer time on the order of months.<sup>22</sup> Hence the goal of the present work is to develop a testing procedure that accelerates the degradation of thermal greases for rapid evaluation of reliability. To accomplish this, we add forced mechanical cycling while holding the thermal grease with a fixed heat flow. Mechanical cycling directly imposes mechanical stresses on the thermal greases (which are at elevated temperatures with temperature gradients), which accelerates the degradation compared to relying on thermal stresses alone as in traditional power cycling tests (due to CTE mismatch) or within electronic packages.<sup>31</sup>

Mechanical cycling has been used previously for studying the degradation of thermal greases. For instance, Chiu et al. <sup>22</sup> subjected thermal greases to mechanical cycling using a Material Test Systems (MTS) universal testing machine with a custom fixture that enabled periodic oscillation of the heat sink assembly between two fixed BLTs to investigate pumpout phenomenon. The thermal grease was subjected to mechanical oscillating while maintaining different heat dissipation (power) levels and enhanced degradation was observed with increasing power. The accelerated tests resulted in degradation within a few hours as opposed to months in a power cycling test of the thermal grease. In addition, Nnebe and Feger <sup>24</sup> studied dryout qualitatively within thermal greases by subjecting them to combined thermal and mechanical cycling. They leveraged infrared (IR) microscopy to observe 'drainage pipes', which are pathways formed within thermal greases for the polymer matrix to escape. These drainage pipes facilitated phase separation and degradation of thermal greases due to dryout. Finally, Carlton et al. <sup>23</sup> performed mechanical cycling of thermal greases at different strains with fixed temperatures of 50 °C and 80 °C. Their study revealed enhanced degradation with increased temperature and strain levels.

Building on these efforts, in the present study, we develop a technique to accelerate the degradation of commercial thermal greases using mechanical cycling and correlate the observed degradation behavior with thermal grease material properties of interest characterized in-house at BOL. Specifically, we perform *in situ* thermal imaging by leveraging high-resolution IR microscopy to investigate and quantify degradation. IR microscope helps

us image the thermal grease degradation while the sample is in the rig with mechanical cycling. Since, IR cameras are widely available at low costs (\$1000 or less), the accelerated testing technique we propose is easily translatable to researchers. We evaluate three different commercial thermal greases having differing thermal and rheological properties at two different initial squeezing pressures (i.e., the pressure required to squeeze the thermal grease before starting the mechanical cycling). The mechanical cycles last for 6 hours and we report the performance metrics at the end-of-experiment (i.e., after 6 hours of mechanical cycling) as end-of-life (EOL). The overall performance of the thermal grease is quantified by assessing its mechanical reliability (by measuring void fraction,  $\phi$  at EOL) and thermal reliability (by comparing EOL and BOL area-normalized thermal resistances,  $R''_{EOL}$  and  $R''_{BOL}$ , respectively). Finally, we conclude this study by uncovering the synergy of material properties that a thermal grease must possess to ensure high mechanical and thermal reliability that will help mitigate the thermal resistance bottlenecks. However, one must note that the present study does not correlate the degradation from accelerated testing to traditional methods such as thermal cycling. Such correlations between the two testing methodologies are important and will be addressed in future studies.

# Experimental methodology

The following sub-sections describe details of the experimental testing including the design and operation of the mechanical cycling test fixture, followed by the thermal image analysis workflow we adopt in the current study to obtain 2D heat flow maps from an input 2D temperature maps to calculate area-normalized thermal resistance.

### Design of the mechanical cycling test fixture

A state-of-the-art mechanical cycling test setup was designed and machined as shown in Fig. 1. The thermal grease is sandwiched between a heated substrate (that moves during the mechanical cycling tests) and a stationary and cooled reference bar. The thermal grease is stencil-printed (using a squeegee to achieve a uniform thickness) on top of the stainless steel reference bar. The stencil has a circular opening of 5 mm and thickness of 0.1 mm. The stencil approach enables consistent dispensing of the same volume of thermal grease across different tests. After dispensing, the thermal grease is squeezed to a specified pressure (measured by load cells) by the heater, insulation, and linear stage assembly. The following subsections describe the two key assemblies: (1) the heater, insulation, and linear stage assembly and (2) the reference bar and cold plate assembly. Additional details on the design of the test fixture can be found in our previous work. <sup>31</sup>

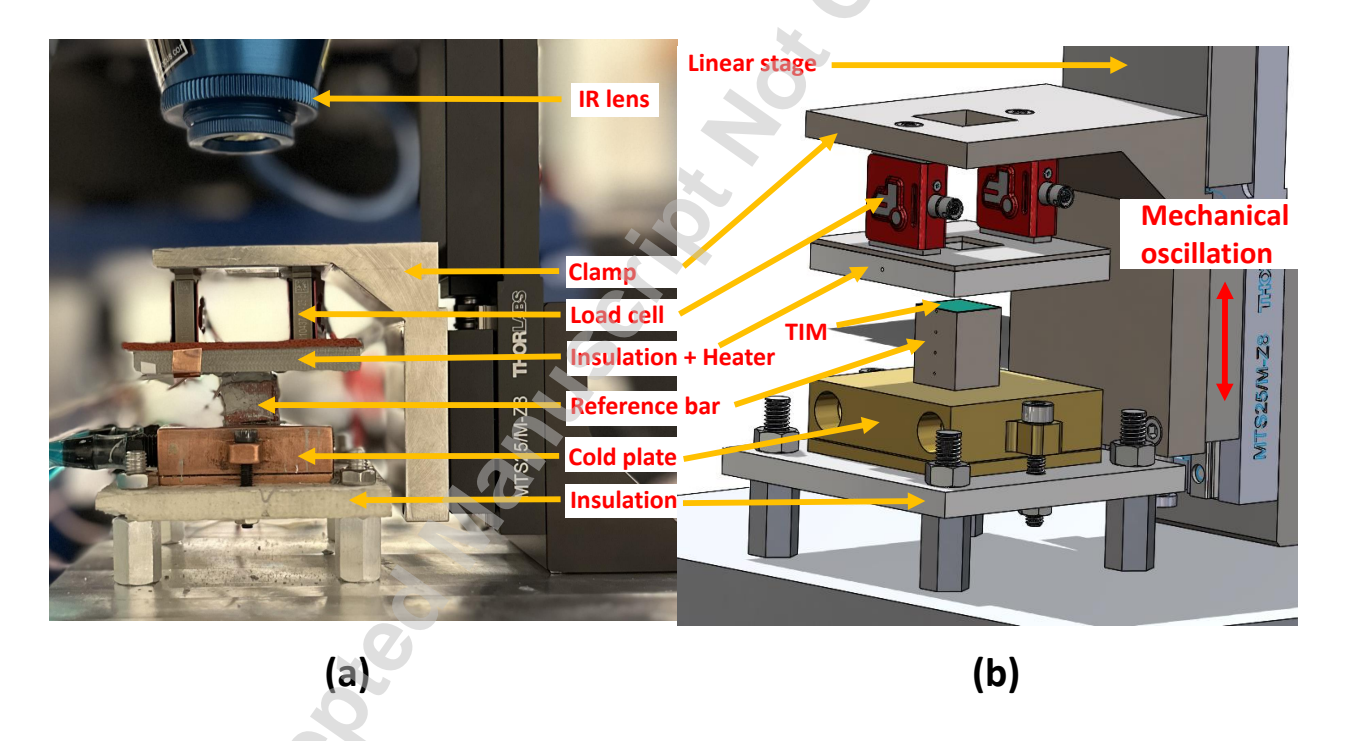


Figure 1: (a) Photograph and (b) CAD model of the accelerated test fixture. The TIM is sandwiched between the heater and the reference bar. The linear stage mechanically oscillates the heater assembly (consisting of the clamp, load cells, and insulation-heater components) with high precision. Simultaneously, a fixed temperature gradient is established across the sample (from the heater to the reference bar that connects to the cold plate). Two load cells integrated into the assembly enable squeezing to the desired nominal pressure (and, thus, control of the BLT) and monitoring of the pressure throughout cycling. The IR camera (lens visible in the image) measures the temperature at the top surface of TIM enabling analysis of void formation and local variations in R''.

#### Heater, insulation, and linear stage assembly

Mechanical oscillations are facilitated by a high-precision linear stage from Thorlabs (P/N: KMTS25E/M - 25 mm). The linear stage is connected to the L-shaped clamp which translates the oscillations from the linear stage onto the load cells (FUTEK LSB205-FSH04097) and heater-insulation subassembly. The heater-insulation subassembly houses the heater within the insulation (fabricated from FR-4) and moves together as a single unit along with load cells and an L-shaped clamp connected to the linear stage. Fig. 2 shows the heater and insulation assembly. The FR-4 insulation protects the load cells from the elevated temperatures of the heater and encourages heat flow through the thermal grease to the reference bar/cold plate. Fig. 2 illustrates the heater and insulation assembly.

Within this assembly, the heater consists of an IR-transparent substrate with a coating to provide heating while enabling thermal imaging of the thermal grease. In the wavelength range of the IR microscope  $(2-5 \mu m)$ , sapphire has a transmission of  $\approx 85\%$  and reflectivity of less than 10% and is selected for the heater substrate.

A cured carbon ink (Creative Materials, 126-28 Low Resistance Carbon Ink) is deposited

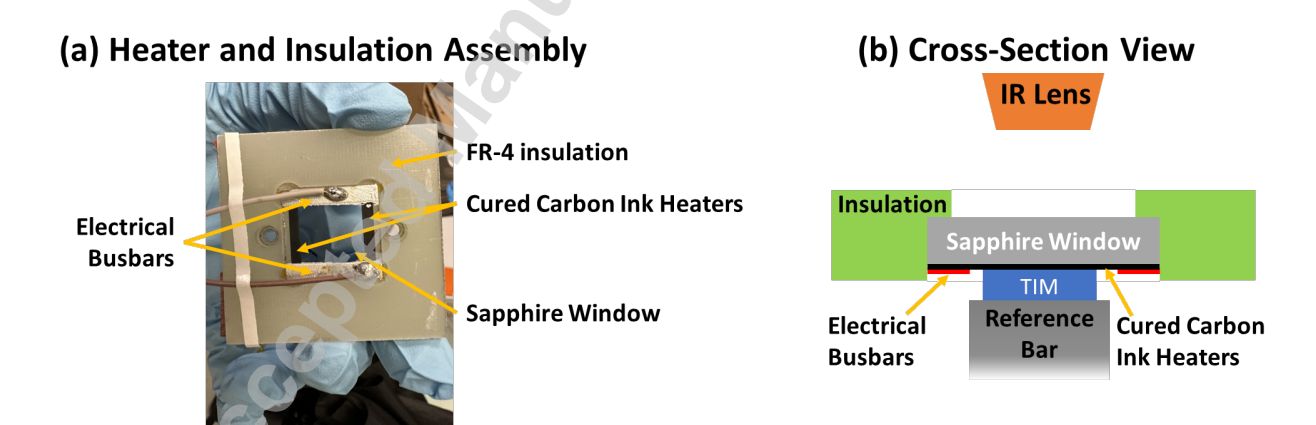


Figure 2: (a) Bottom-view photograph and (b) cross-sectional schematic of the heater and insulation assembly. Current flowing through the silver bus bars to the carbon ink lines at the edge of the window generates heating. This heat conducts both in-plane through the sapphire substrate and vertically through the TIM to the cooled reference bar. The sapphire window also enables IR imaging of the in-plane temperature distribution within the TIM during mechanical cycling. The FR-4 insulation protects the load cells from the heat and guides the heat to flow through the TIM.

on a sapphire window in a ring shape to act as a heater. In other words, the carbon ink is screen printed in a  $\sim 2.5$  mm strip along each of the 4 outer edges of the sapphire window, so that the center portion of the sapphire window enables thermal imaging directly at the top surface of the thermal grease. Hence, we call the heater in the current setup a "ring heater". After deposition, the carbon ink is cured in an oven at 180 °C for 15 min present underneath the sapphire window at the four edges.

Next, silver busbars (MG Chemicals, 8331D Silver Conductive Epoxy Adhesive) are painted onto two edges of the sapphire substrate overlapping the carbon ink at those edges. The silver paint enables good contact with the carbon ink heater when wires are soldered to the heater. The wires are connected to a DC power supply to enable Joule heating of the cured carbon ink from the other two edges which are not covered by the silver busbars.

Given the edge heater pattern, the heating is non-uniform, with heat generation focused at the edges (where the carbon ink is present). Therefore, the temperature maps of thermal grease have an in-plane temperature gradient with higher temperatures on the edges and lower temperatures in the center.

#### Reference bar and cold plate assembly

The stainless steel reference bar (with a  $12 \times 12 \text{ mm}^2$  cross-section and 12 mm height) is soldered on top of a copper cold plate (Custom Thermoelectric, WBA-1.62-0.55-CU-01) through which water-ethylene glycol coolant flows. The reference bar and cold plate together act as a heat sink. The cold plate is fixed on top of a sheet of Macor insulation that acts as a base for the test structure.

The reference bar contains four holes to insert T-type thermocouples to measure the variation of temperature along the position. Based on Fourier's Law, the measured temperature gradient and known thermal conductivity  $(14 \text{ W/(m K)}^{32})$  enable quantification of the global heat flux passing through the thermal grease into the heat sink and estimation of the temperature of the top surface of the reference bar or bottom surface of thermal grease.

### Mechanical cycling methodology

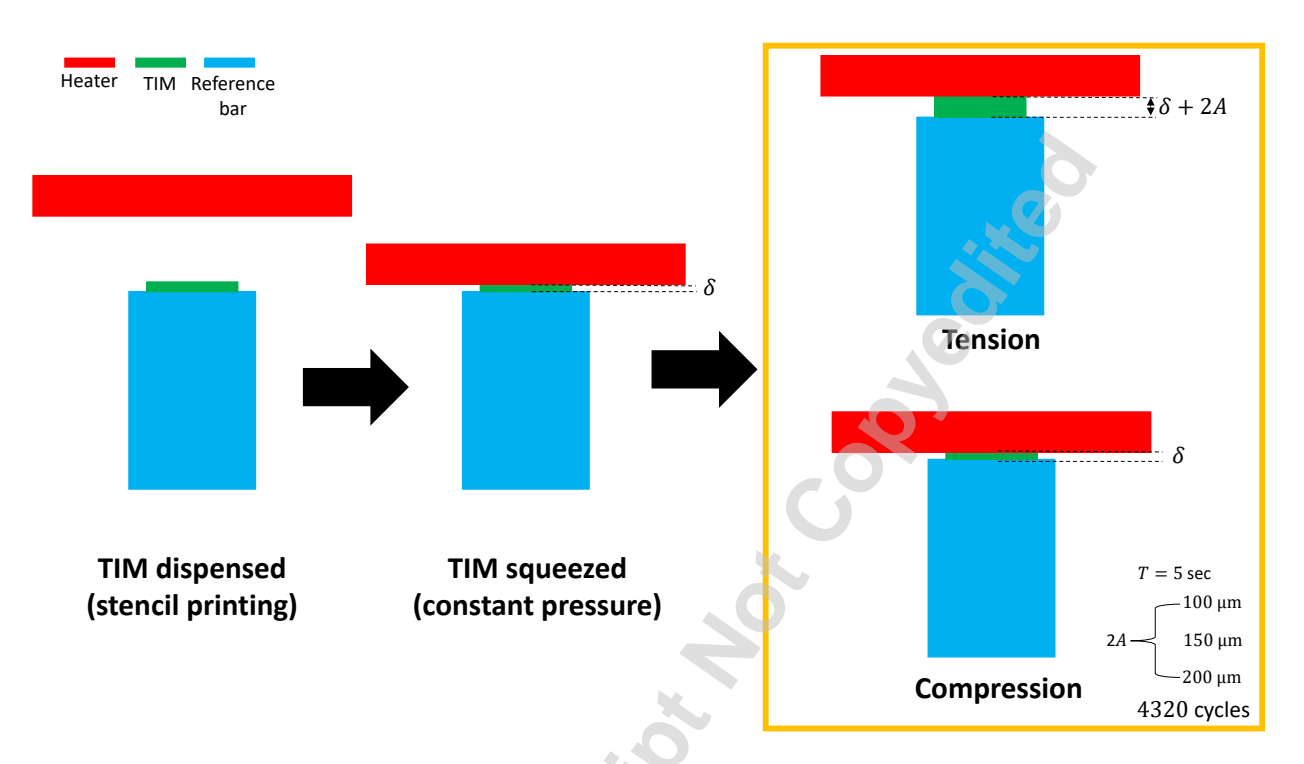


Figure 3: The mechanical cycling methodology employed in the present work to facilitate accelerated degradation of thermal greases. After squeezing the thermal grease at a constant pressure to a BLT  $\delta$ , the thermal grease is subjected to repeated tension and compression cycles for 6 hours (or 4320 cycles).

The approach for mechanical cycling of thermal greases to facilitate accelerated degradation is shown in Fig. 3. First, we squeeze the thermal grease to a constant pressure (0.075 MPa or 0.15 MPa) which results in an initial BLT of  $\delta$ . This is achieved by lowering the linear stage until the desired pressure is reached as measured by the load cells. Next, we subject the thermal grease to tension forces to reach a BLT of  $\delta + 2A$ , where  $2A = 100 \ \mu\text{m}$ ,  $150 \ \mu\text{m}$ ,  $200 \ \mu\text{m}$  is the amplitude of mechanical oscillations. Finally, we subject the thermal grease to compression force by squeezing it back to the initial BLT of  $\delta$ . The total motion distance the thermal grease is subjected to is 2A, where A is the oscillation amplitude. This process is repeated for 4320 mechanical cycles over the course of 6 hours. The time period of each mechanical cycle is held fixed at 5 s. Every 2 hours, the cycling is paused so that a steady state temperature map of the top surface of thermal grease can be

captured. Finally, an IR movie spanning the entire testing period is recorded by capturing a frame every 5 mins to analyze the evolution of thermal grease degradation. It must be noted that in our current fixture configuration, it is not possible to measure the BLT  $\delta$  that is achieved by squeezing the thermal grease at constant pressure. We control the oscillation amplitude A in our experiments.

Note that we chose the applied pressures to be 0.075 MPa and 0.15 MPa to mimic realistic squeezing pressures of 0.035 – 1.03 MPa within electronic packages. <sup>12</sup> Typically, the lower end of the squeezing pressure range ( $\sim$ 0.075 MPa) represents higher BLT applications such as in power electronics, <sup>33</sup> while higher squeezing pressures ( $\sim$ 0.15 MPa) target the microprocessor chip squeezing. <sup>22</sup> Squeezing pressures for thermal gap pads can range from 40-50 psi (0.27-0.35 MPa) or higher to achieve optimal performance. But, thermal greases, being softer, attain their desired bondline of 20-50  $\mu$ m at lower pressures and hence we chose 0.075 MPa and 0.15 MPa for our tests. In addition, a high amplitude of squeezing (100-200  $\mu$ m) was selected to ensure the thermal greases degrade within 6 hours of testing to enable acceleration of the degradation analysis. The thermal greases chosen in the current work are less "degradation prone" (according to the manufacturer) and have been released into the market within last one year. We tested the accelerated degradation at a range of squeezing amplitudes and found reasonable degradation times (*i.e.*, 6 hours) for 100, 150, and 200  $\mu$ m.

### Thermal image analysis

To investigate the degradation in reliability performance in situ, 2D temperature maps of the interfacial surface between the thermal grease and an infrared (IR)-transparent substrate are captured using IR microscopy every 2 hours at steady-state conditions (by pausing the mechanical cycling). From these thermal images, we quantify mechanical and thermal reliability performance metrics by calculating the void fraction ( $\phi$ ) at EOL and area-normalized thermal resistance (R'') at BOL and EOL, respectively. It must be noted that the thermal grease is dispensed using a stencil of 5 mm diameter and 100  $\mu$ m thickness (before squeezing) across the different tests and hence the void fraction at BOL is negligible.

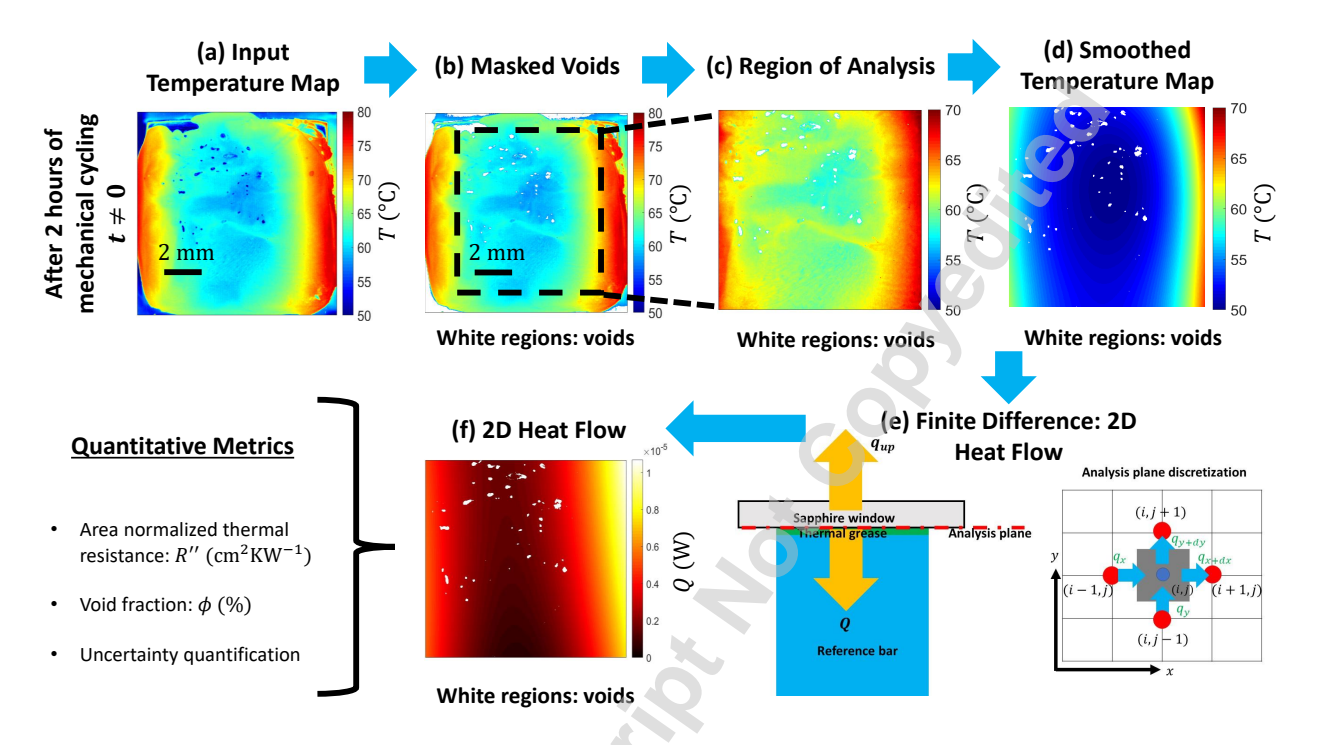


Figure 4: Workflow to obtain 2D heat flow maps from the input IR temperature maps at steady state. (a) The input temperature maps (containing voids due to mechanical cycling). (b) These voids are masked (by assigning them NaN values to appear white). (c) Next, the image is cropped to a central  $700 \times 700$  pixel  $(8.5 \times 8.5 \text{ mm}^2)$  region of analysis. (d) Due to inherent noise in the thermal images, the temperature map is smoothed (via a polynomial surface fit) to improve the evaluation of the derivatives needed to characterize heat flow rates. (e) Due to non-uniform heating by the ring heater, a finite difference scheme is used to discretize the heat diffusion equation to obtain the (f) 2D heat flow map from the smoothed temperature maps. Finally using the smoothed temperature map and calculated 2D heat flow map, relevant metrics of performance and degradation are quantified (such as area-normalized thermal resistance (R'') and void fraction  $(\phi)$ ).

As mentioned in Sec. Design of the mechanical cycling test fixture, we use a "ring" heater consisting of a cured carbon ink patterned on an IR-transparent window to facilitate heating at fixed power levels throughout the mechanical cycling. The ring heater causes non-uniform heating of thermal greases due to Joule heating in two resistive carbon ink strips at the edges of the IR-transparent window. Hence, an in-plane temperature gradient exists in steady-state temperature maps captured from IR measurements (see Fig. 4(a)). Due to

non-uniform temperature distribution, we post-process the images in MATLAB R2019 to obtain 2D heat flow maps, from which we can calculate the global area-normalized thermal resistance value (R''). An example of post-processing workflow on one of our steady-state temperature maps is shown in Fig. 4.

For this illustration, we consider a steady-state temperature map for TIM-A after two hours of mechanical cycling (Fig. 4(a)). In these images, voids (i.e., regions with no thermal grease) appear significantly colder than the thermal grease in the IR measurement because the reference bar is directly imaged in these regions while the emissivity calibration assumes the thermal grease is still present. Specifically, the thermal greases have higher emissivity (refer to the section on Infrared Imaging of Thermal Grease) compared to the stainlesssteel reference bar (present beneath the thermal grease) and, thus, even at relatively similar temperatures, the voids appear significantly darker/colder in the IR images. We perform pixel-by-pixel comparison and demarcate the regions with  $T_{\rm IR}-T_{\rm ref-bar}<0$  as voids, where  $T_{\rm IR}$  is the IR temperature and  $T_{\rm ref-bar}$  is the temperature of the bottom surface of thermal grease (or top surface of reference bar) obtained by linear interpolation of temperatures as a function of position. The voids are assigned a value of NaN and, hence, appear as white regions in the processed image (Fig. 4(b)). Next, to avoid edge effects and to focus the entire region of analysis within the area with thermal grease, we crop the temperature map into the central  $8.5 \times 8.5 \text{ mm}^2$  (or  $700 \times 700 \text{ pixel}$ ) region (Fig. 4(c)). The resulting temperature map has noise (inherent to any temperature measurement) that impacts the calculation of the derivatives required to estimate the heat flow rates. To circumvent this problem, we smooth the temperature map (Fig. 4(d)) using a polynomial surface fit in MATLAB R2019. Due to the edge heating, the temperature map has an approximately parabolic shape in the 2D plane, and hence, poly44 surface fit captures the temperature profile with good accuracy. Next, we consider a discretized energy balance on each pixel of the thermal image considering steady-state heat transfer to calculate the 2D heat flow map (Fig. 4(e-f)). Detailed mathematical analysis is found in the appendix of our previous work. <sup>31</sup> Finally, using the smoothed temperature map ((Fig. 4(d)) and the 2D heat flow map in ((Fig. 4(f)), we calculate the pixel-by-pixel area-normalized heat conductance values and sum them up to find the global area-normalized heat conductance (h'') for the steady-state temperature map under consideration. Finally, we calculate the averaged area-normalized thermal resistance (R'' = 1/h'') to quantify the thermal performance of the thermal grease. Finally, we consider the propagation of uncertainty in our estimates of void fractions and thermal resistance assuming an uncertainty in the temperature measurements ( $T_{IR}$  and  $T_{ref-bar}$ ) of  $\pm 1$  °C.

### Results and discussion

Thermal greases are complex soft matter possessing non-Newtonian rheology <sup>19,21</sup> and, hence, it is important to characterize their viscoelastic and thermal properties to quantify their degradation behavior from a fundamental point of view. In this section, we first introduce the material properties of three different commercial thermal greases that were characterized in-house. Next, we analyze the impact of the initial squeezing pressures and thermal grease rheology on the performance and degradation metrics.

# Thermal grease material properties

First, we perform small amplitude oscillatory shear (SAOS) tests to characterize the storage (or elastic) modulus (G') and loss modulus (G'') of thermal greases. The G' and G'' are typically measured before the material yields and represent the ability of thermal grease to store and dissipate energy respectively, when subjected to thermo-mechanical stresses within an electronic package. We calculate structured viscosity as  $\eta_s = G''/\omega$  to represent the dissipative behavior that is usually associated with viscosity. <sup>34</sup> Next, we use flow curve experiments to characterize the flow properties [plastic viscosity ( $\eta_p$ ) and yield stress ( $\sigma_y$ )] of thermal grease post-yielding by fitting a Bingham plastic model to the data. Finally, the thermal conductivity of the thermal greases is characterized using transient hotwire experi-

ments. The measured rheological and thermal properties are listed in Table 1 and details of the approaches undertaken to characterize these properties are listed in Appendix Appendix.

Three thermal greases under consideration were chosen for our mechanical cycling experiments because of their differing properties to uncover the effect of the rheological and thermal properties on degradation. Here, we will use the designations TIM-A, TIM-B, and TIM-C, to refer to the three materials. Specifically, TIMs A and B have higher values of storage modulus (G') and thermal conductivity (k) than TIM-C. However, the ratio  $G'/\eta$  is highest for TIM-C. Here, we calculate the ratio  $G'/\eta$  using the structured viscosity ( $\eta_s$ ) for TIM-A and TIM-B and the post-yield flow viscosity ( $\eta_p$ ) for TIM-C. Because TIM-C has a lower yield stress, it deforms easily under mechanical cycling loads motivating our use of the flow viscosity  $\eta_p$ . In contrast, TIM-A and TIM-B demonstrate pre-yield behavior under mechanical cycling due to the high yield stress. Note that the proposed metric to evaluate TIM performance (the ratio  $G'/\eta$ ) is equivalent to that proposed by Prasher and Matayabas <sup>11</sup>: G'/G''.

# Mechanical cycling of thermal greases

In this section, we explain the impact of initial squeezing pressures and thermal grease rheology on the reliability of TIMs-A, B, and C by subjecting them to mechanical cycling at fixed power levels to accelerate the degradation process.

Table 1: Rheological thermal properties of thermal greases considered in the present study.

Material Property	TIM-A	TIM-B	TIM-C
G' (Pa)	9398	10242	287
$\eta_s \; (\mathrm{Pa}\mathrm{s})$	2409	1181	69
$\sigma_y (\mathrm{Pas})$	181	85.9	29.7
$\eta_p \; (\mathrm{Pas})$	144.1	68.1	7.5
$G'/\eta \ ({\rm s}^{-1})$	3.9	8.7	38.3
k (W/m/K)	5.6	4.6	3.9

#### Effect of initial squeezing pressure

Electronic packages have a range of target BLTs for different applications leading to different gap thicknesses that the thermal grease must fill to reduce the interface thermal resistance. For example, within power module packages, the BLT can be large ( $\sim 1 \text{ mm}$ ). On the other hand, within microprocessor packages, the BLTs are much smaller ( $\sim 20-50~\mu\text{m}$ ). <sup>22</sup> In the present study, we investigate the impact of different BLTs on thermal grease degradation by conducting experiments at two different initial squeezing pressures: 0.075 MPa and 0.15 MPa for TIM-A. The initial squeezing pressures after dispensing the TIM-A determines its BLT (in addition to the rheological properties).

For TIM-A, the EOL 2D IR temperature maps at two different squeezing pressures are shown in Fig. 5. As we go from left to right, the mechanical oscillation amplitude increases from 100  $\mu$ m to 150  $\mu$ m to 200  $\mu$ m resulting in enhanced degradation as seen from the large voids (white regions). At lower squeezing pressure of 0.075 MPa (resulting in higher BLT), more degradation is seen. That is, there is a higher void fraction and evidence of pumpout (*i.e.*, movement of the thermal grease out of the interface). In contrast, at higher squeezing pressure of 0.15 MPa (lower BLT), the degradation is reduced, however, with increasing amplitude of the mechanical oscillations, the degradation increases resulting in poor thermal grease performance.

The overall reliability of the thermal grease is further quantified in Fig. 6 where we report the EOL void fractions and the evolution of the thermal resistances at two different initial squeezing pressures. As expected, at both initial squeezing pressures, the mechanical and thermal reliability generally decreases with increasing oscillation amplitude due to an increase in void fractions and the ratio of  $R''_{\rm EOL}/R''_{\rm BOL}$  with A. Higher amplitudes increase the agitation of thermal grease causing it to perform poorly. Further, the void fraction and EOL thermal resistance increase more significantly at the lower initial squeezing pressure (0.075 MPa) indicating poorer mechanical and thermal reliability for lower initial squeezing pressure (higher BLT). At low oscillation amplitudes (100  $\mu$ m and 150  $\mu$ m) and higher initial

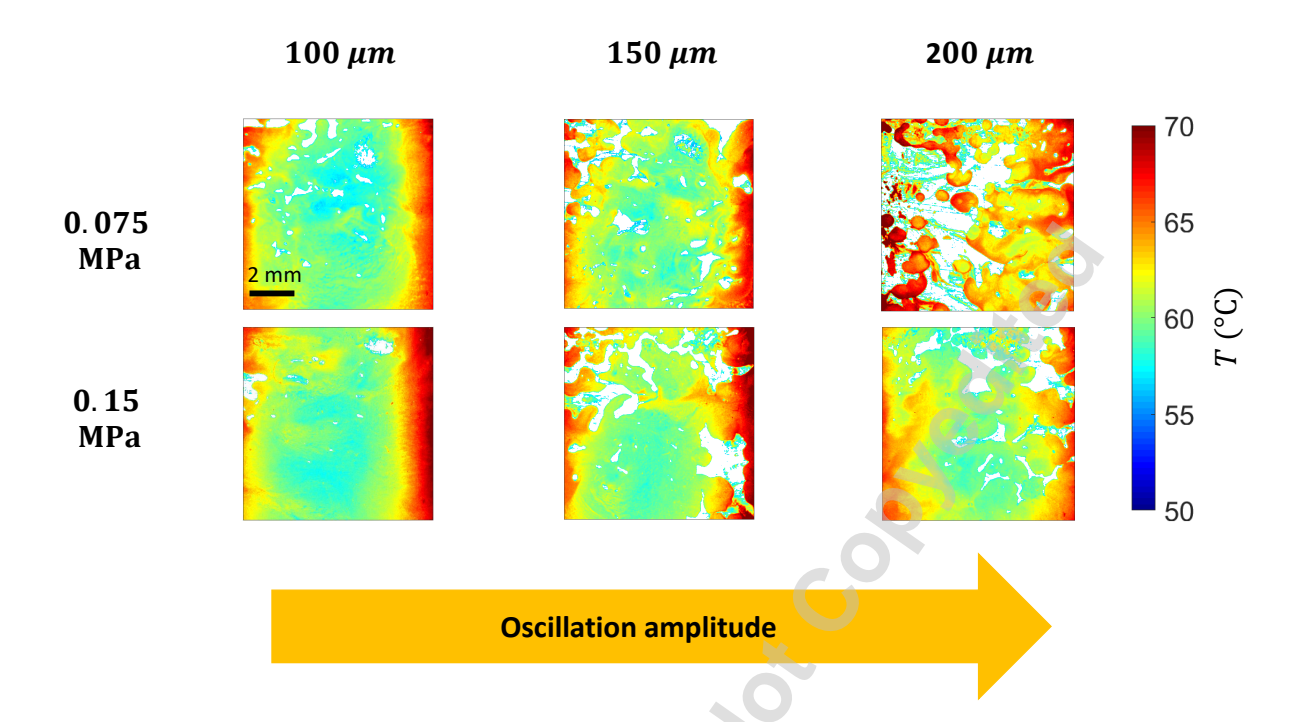


Figure 5: Temperature maps captured from IR microscope at EOL for TIM-A. Each row corresponds to a different squeezing pressure and each column corresponds to different amplitudes for the mechanical oscillations (A). Degradation in the form of void formation increases with increasing A for both squeezing pressures due to enhanced mechanical agitation of the TIM-A. Further, the degradation is more pronounced for lower squeezing pressure due to higher BLT resulting in a higher viscosity gradient along the BLT, which causes more voids to open.

squeeze pressure (0.15 MPa), the thermal reliability of TIM-A improves (i.e., R'' reduces from BOL to EOL) likely due to improved spreading of the thermal grease throughout the interface. However, a sharp increase in R'' ( $R''_{\rm EOL}/R''_{\rm BOL}\approx 4$ ) is observed at 200  $\mu$ m for lower squeezing pressure because of higher void percentage and pumpout of the thermal grease. In contrast, the same amplitude of oscillations with a higher initial squeezing pressure results in a less drastic ratio  $R''_{\rm EOL}/R''_{\rm BOL}\approx 1.2$ . The poor mechanical and thermal reliability for TIM-A at lower squeezing pressure is due to larger BLT, which results in a higher temperature drop across the interface. A larger temperature drop has an unintended effect of a larger variation in viscosity across the thickness of the TIM, which causes it to shear and flow easily when subjected to mechanical cycling. Typically, the viscosity of TIM near the sapphire window is lower (due to higher temperatures) than the viscosity near the reference bar <sup>29</sup>. At lower

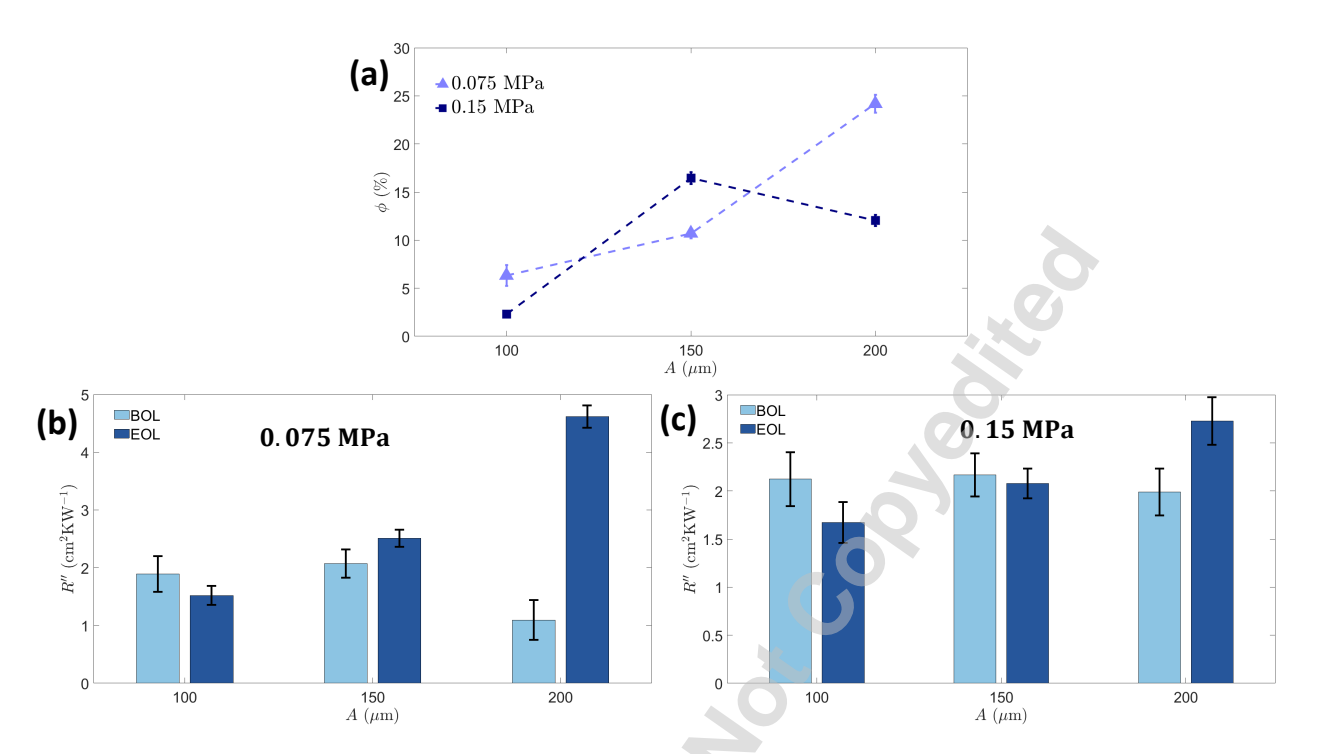


Figure 6: Mechanical and thermal reliability performance of TIM-A across different oscillation amplitudes and initial squeezing pressures. (a) End-of-life void fraction  $\phi$  and evolution of the thermal resistance from BOL to EOL with pressures of (b) 0.075 MPa and (c) 0.15 MPa. At lower squeezing pressure, we observe higher void fractions (poor mechanical reliability) and more significant degradation of the thermal resistance (poor thermal reliability) due to larger variations in temperature and viscosity across BLT, which enhances shearing and exacerbates degradation. The performance at both squeezing pressures degrades with increasing oscillation amplitude due to higher agitation and movement of TIM. Note: the dashed lines serve to guide the eye and do not represent any trends.

squeezing pressure, the viscosity difference across the BLT is larger than for the higher initial squeezing pressure resulting in enhanced relative motion across the TIM thickness causing it to degrade more rapidly.

#### Effect of thermal grease rheology

In this subsection, we compare the effect of thermal grease rheology on its degradation. We expose TIMs-A, B, and C (material properties listed in Table 1) to the mechanical cycles at a fixed squeezing pressure of 0.15 MPa to assess their mechanical and thermal reliability.

Temperature maps obtained at EOL are shown in Fig. 7 for all 3 thermal greases and

at three different oscillation amplitudes:  $100 \ \mu\text{m}$ ,  $150 \ \mu\text{m}$ , and  $200 \ \mu\text{m}$ . The degradation of the thermal grease is clear from the voids and pumpout observed at the EOL. The void fraction increases with increasing amplitude for the mechanical oscillations due to higher perturbation of all thermal greases under consideration. Overall, TIM-A and TIM-B exhibit higher void fractions after testing (hence, exhibiting poor mechanical reliability) compared to TIM-C. To explain the results further, we quantify the void fraction and the thermal resistances in Fig. 8.

Consistent with the temperature maps in Fig. 7, Fig. 8 shows higher EOL void fractions for TIM-A and TIM-B than TIM-C. These thermal greases have a lower ratio of the storage modulus to the viscosity  $G'/\eta$  than TIM-C and, hence, their ability to store thermomechan-

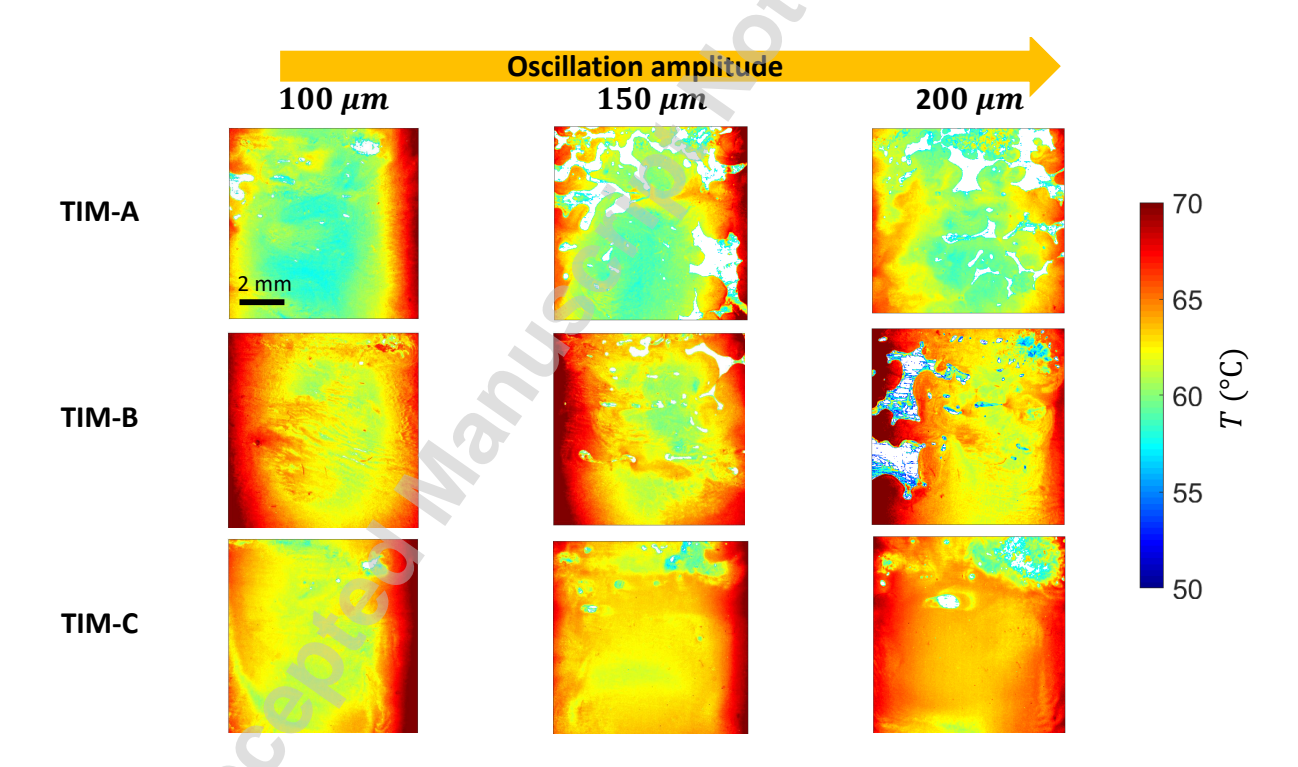


Figure 7: Temperature maps at EOL for all three TIMs at a squeezing pressure of 0.15 MPa. Each row corresponds to a different TIM and each column corresponds to a different oscillation amplitude. TIM-A exhibits high voiding wherein voids are formed predominantly in the center of the interfacial area, while TIM-B has fewer voids primarily located near the edge of the domain. Finally, TIM-C exhibits little to no voiding even at high oscillation amplitudes. For all three TIMs, the voiding increases with higher oscillation amplitudes, due to increased agitation and movement of TIM.

ical stresses (relative to dissipating stresses) is poor causing enhanced void formations. A high  $(G'/\eta)$  ratio for TIM-C indicates a small viscosity value and hence TIM-C flows easily to close the voids that appear during mechanical cycling. Among the three thermal greases, TIM-A has poor mechanical reliability due to the highest void fraction explained by the lowest  $G'/\eta$  (refer to Table 1.)

Interestingly, the thermal reliability is superior for TIM-A and TIM-B (i.e., a lower relative increase of  $R''_{EOL}$  compared to  $R''_{BOL}$ ) compared to TIM-C despite having poor mechanical reliability. This is due to synergy in material properties, with high thermal conductivity (k),

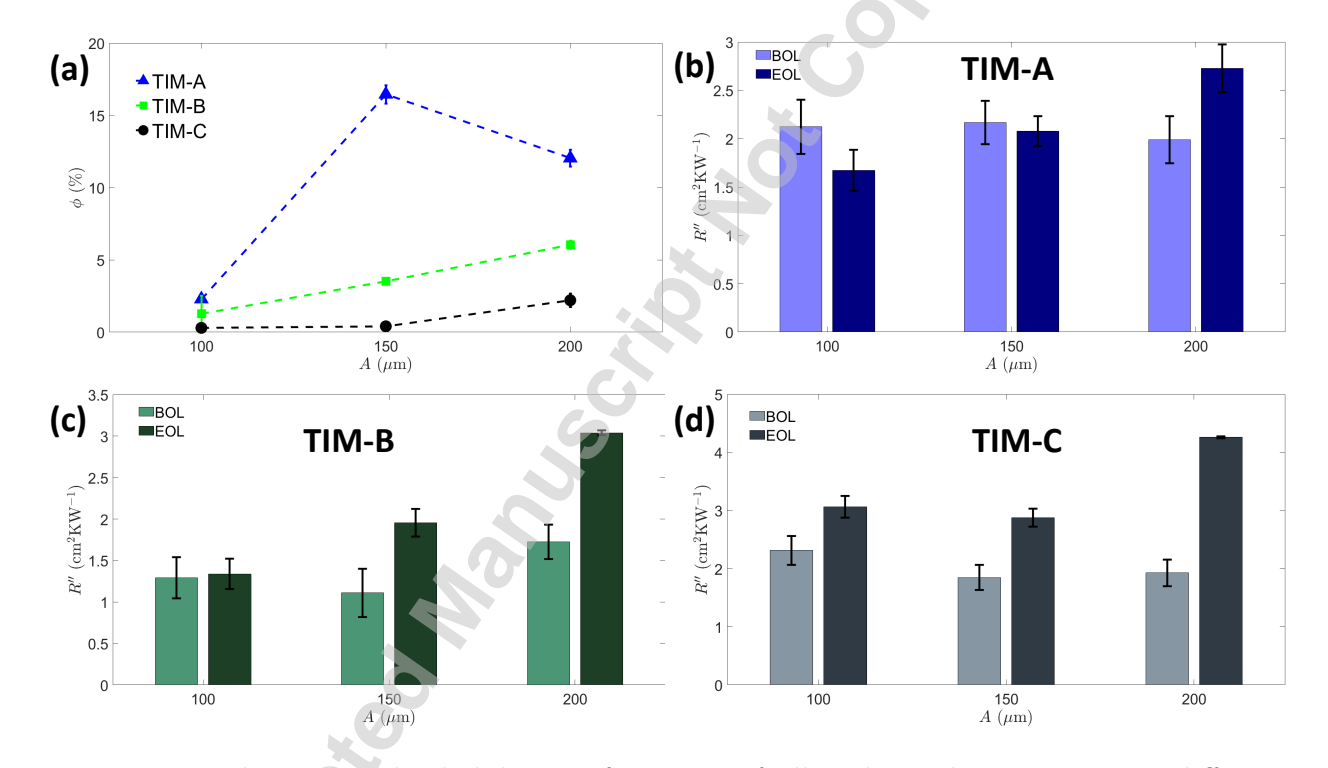


Figure 8: Mechanical and reliability performance of all 3 thermal greases across different oscillation amplitudes at an initial squeezing pressure of 0.15 MPa. (a) End-of-life void fraction  $\phi$  and evolution of the thermal resistance from BOL to EOL for (b) TIM-A, (c) TIM-B, and (d) TIM-C. Due to a higher  $G'/\eta$  ratio for TIM-C compared to the others, it possesses superior mechanical reliability with little to no voiding at the EOL. However, the relative increase in R'' (thermal reliability) is lower for TIMs-A and B due to a combination of high absolute value of G' and high k. In the present non-uniform heating configuration, the location of voids impacts the overall thermal performance: voids at the edges cause much higher local thermal resistances near the local heat sources while the voids near the center are in regions with lower impact on overall thermal performance. Note: the dashed lines serve to guide the eye and do not represent any trends.

and high magnitude of the storage modulus (G') resulting in higher thermal reliability. The higher absolute value of G' of TIMs-A and B indicates their ability to store a much larger amount of thermomechanical stresses (and for a longer duration) compared to TIM-C and, hence, over their accelerated tested lifetime, the relative increase in R'' is lower than TIM-C. While higher k of TIMs-A and B enable better thermal transport across the TIM-C resulting in lower R''. In addition to the elastic modulus and thermal conductivity, the location of voids also impacts the  $R''_{EOL}$ , in particular, due to the non-uniform nature of heating. In the central region, where there is no Joule heating, the temperature difference between the top and bottom surface of thermal grease is very small and only a small fraction of the heat is conducted across the thermal grease in this region. Hence, voids formed in the central unheated region have little to no impact on the overall thermal conductance of the thermal grease (and, hence,  $R''_{EOL}$ ). However, the voids formed near the heated edges have a higher contribution to overall thermal conductance (and, hence, thermal resistances). Near the edges, the temperature difference across the thermal grease is large and this region carries much of the heat flow across the thermal grease. Therefore, voids formed near the edges can hinder local thermal grease thermal conductance much more effectively than the voids formed in the center for this heater configuration. As observed from IR temperature maps in Fig. 7, much of the voiding in TIM-A is in the center region, and, hence, the high void fraction does not drastically increase the thermal resistance. Furthermore, TIM-B exhibits a lower percentage of voids near the edges, resulting in overall better thermal reliability.

Further, at lower oscillation amplitudes, TIMs-A and B are also seen to improve due to their ability to fill the interface entirely displacing the trapped air out of the interface. Thus, based on these results, we emphasize that thermal grease with good mechanical reliability may not possess good thermal reliability (and vice-versa) due to the dependence on multiple material properties.

### Conclusion and Future Work

In this work, we demonstrate a method for accelerating the degradation testing of thermal greases leveraging mechanical cycling to induce degradation quicker than with traditional thermal or power cycling tests. For three commercial thermal greases at two different initial squeezing pressures of 0.075 MPa and 0.15 MPa, degradation occurs within 6 hours, rather than weeks to months with power cycling. We further characterize rheological and thermal properties of interest including in-house to correlate the degradation behavior of thermal greases with the material properties.

Infrared temperature maps enable quantification of the mechanical reliability (through the EOL void fraction) and thermal reliability (comparison of  $R''_{\rm BOL}$  to  $R''_{\rm EOL}$ ). Our results for TIM-A show that lower squeezing pressure (higher BLT) results in larger temperature and viscosity variation across the interface compared to higher squeezing pressures (lower BLT). Higher viscosity variation across the BLT facilitates shearing causing easy flow of the thermal grease resulting in poor mechanical and thermal reliabilities. Further, the rheological properties of thermal grease also have a vital effect on its reliability. The ratio of storage modulus to viscosity  $(G'/\eta)$  governs the ability of thermal grease to store the thermomechanical stresses over dissipating it and a higher ratio for TIM-C resulted in better mechanical reliability (i.e., less void formation). Further, the thermal reliability is demonstrated by the change in R'' over the lifetime of thermal grease. The EOL thermal resistance was sensitive to the location of voids (due in part to the non-uniform nature of heating). Our experiments uncover that a combination of high thermal conductivity (better thermal transport), high elastic modulus (larger and longer thermomechanical stress storage), and void formation in the central region for TIMs-A and B resulted in better thermal reliability. Hence it must be noted that thermal grease with high mechanical reliability does not ensure high thermal reliability due to dependence on different material properties (and vice-versa). A combination of high elastic modulus to viscosity ratio, the absolute value of elastic modulus, and thermal conductivity can be used to design thermal greases that have high mechanical and thermal reliability.

Since thermal greases are complex non-Newtonian fluids, their material properties likely change with mechanical cycling due to the repositioning of filler particles (*i.e.*, changes in microstructure). Hence, more accurate insights on thermal grease degradation can be developed if material properties can be characterized at EOL to compare the percentage change in their values from BOL. In addition, a direct correlation between void fraction and thermal resistance can be observed if a uniform heater coating (such as the indium-tin oxide) on an IR-transparent window is used that facilitates IR imaging of thermal grease. Finally, it is important for further studies to compare the accelerated degradation testing results to long-term studies of degradation using power or thermal cycling in order to project lifetime performance from the new test process. Currently, the relation between the accelerated tests proposed in this work to that of traditional tests (thermal cycling) is unknown.

Overall, this accelerated testing method shows promise for increasing the throughput of thermal reliability testing for thermal greases, which could lead to faster development of new materials and more data to understand the mechanisms that lead to high reliability.

# Acknowledgements

Financial support for this work provided, in part, by members of the Cooling Technologies Research Center, a graduated National Science Foundation Industry/University Cooperative Research Center at Purdue University, is gratefully acknowledged.

P. Nagrani gratefully acknowledges the support of the Bilsland Fellowship through Purdue University.

We thank Prof. Ivan Christov for helpful discussions regarding the pressure-driven flow of TIMs subjected to mechanical cycling. We further thank Prof. Kendra Erk for helpful discussions on SAOS rheology tests and for access and training on the parallel plate rheometer to characterize the thermal grease rheology.

# Data availability

Data will be made available on request.

# **Appendix**

### Characterization of Rheological Properties of the Thermal Greases

To characterize the viscoelastic properties of thermal greases, SAOS experiments are performed using an Anton Paar parallel plate rheometer with a nominal gap height (i.e., thickness of the thermal grease) of 150  $\mu$ m while sweeping through the amplitudes and frequencies of oscillations. For the data in Fig. 9, the temperature was fixed at 60 °C, which represents the approximate temperature of the bottom surface of thermal grease and the top surface of the reference bar during testing. Further, temperature sweeps from 60 °C to 100 °C (the temperature of top surface of thermal grease during mechanical cycling) showed no significant variation in material properties.

An amplitude sweep test from 0.01% to 100% strain at a frequency of 10 rad/s enables identification of the linear viscoelastic regime (LVER) by determining the crossover point of the G' and G'' curves. As seen from Fig. 9(a), all the thermal greases have crossover points at strains higher than 0.1% and, hence, 0.1% was chosen as the amplitude for the frequency sweep tests showing in Fig. 9(b). In those tests, the frequency was varied from 1 rad/s to 628 rad/s to see the variation of G' and G''. The rheological properties (G' and structured viscosity  $\eta_s = G''/\omega$ ) are calculated at  $\omega = 1.25$  rad/s, since this frequency translates to a period of 5 s that is used for the accelerated degradation experiments. The elastic properties of thermal grease before degradation (i.e., within the LVER range) are characterized by G' and  $\eta_s$ . While only one set of data is plotted in Fig. 9, the experiments were repeated three times in the interest of considering variations in the thermal grease samples. Average values of the extracted G' and  $\eta_s$  from the 3 runs (at a frequency of  $\omega = 1.25$  rad/s) are reported

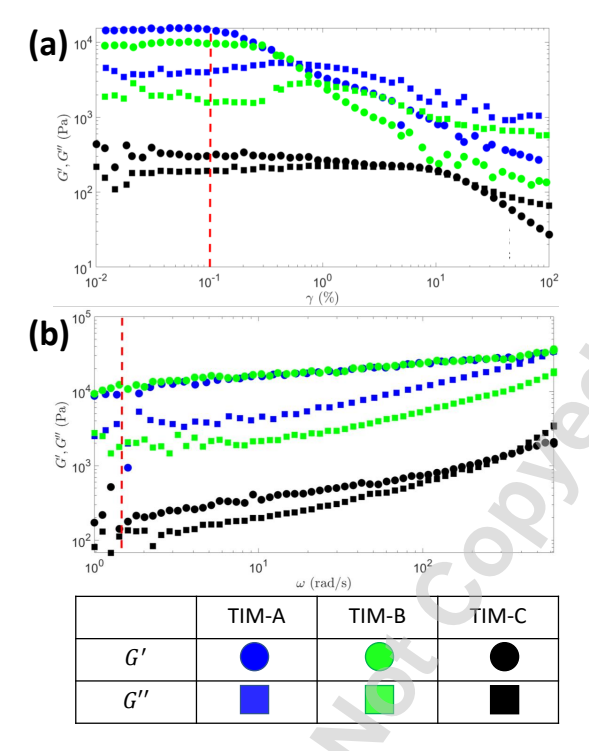


Figure 9: Storage (G') and loss (G'') moduli of three commercial thermal greases based on SAOS rheology tests in a parallel-plate rheometer at 60 °C temperature and 150  $\mu$ m gap height. (a) Amplitude sweep (from 0.01% to 100% strain at a frequency of 10 rad/s) and (b) Frequency sweep from 1 rad/s to 628 rad/s at an amplitude of 0.1%. The amplitude sweep illustrates that the crossover points for G' and G'' for all three thermal greases are at strains greater than 0.1% (vertical dashed red line). The mechanical cycling degradation tests are performed at  $\omega = 1.25$  rad/s (vertical dashed red line in panel (b)). Thus, relevant properties (G') and  $\eta_s = G''/\omega$  are reported at this frequency.

#### in Table 1.

Next, using the same Anton Paar parallel plate rheometer at a nominal height of 150  $\mu$ m and temperature of 60 °C, we perform flow curve tests by ramping the shear rate up from  $0.01 \text{ s}^{-1}$  to  $100 \text{ s}^{-1}$  and fit a Bingham plastic model ( $\sigma = \sigma_y + \eta_p \dot{\gamma}$ , where  $\dot{\gamma}$  is the imposed shear rate and  $\sigma$  is the measured shear stress) as shown in Fig. 10. Each data point was obtained after waiting for 10 s to reach steady state conditions. The model is fit to the data to extract material properties of interest ( $\sigma_y$  and  $\eta_p$ ) to characterize the post-yield behavior. In the present work, we obtain highly accurate curve fits ( $R^2 > 0.98$ ) by assuming thermal grease to follow a rheological model for a Bingham plastic. Extracted properties for thermal greases are listed in Table 1.

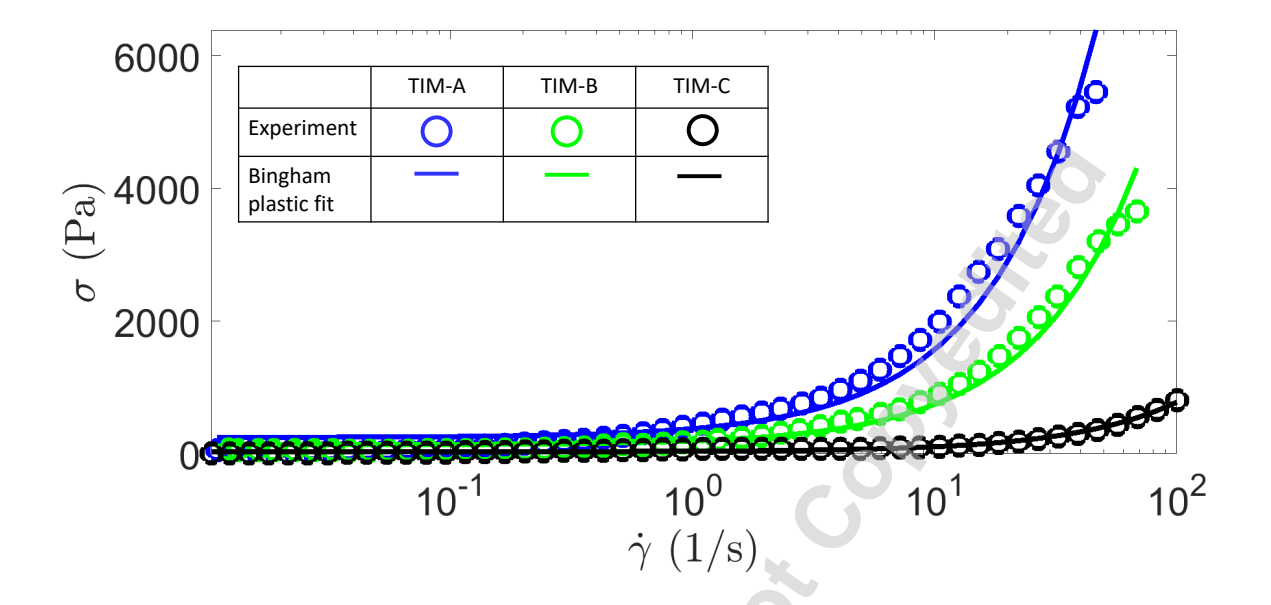


Figure 10: Flow curves for TIMs-A, B and C at 60 °C to characterize the post-yield properties  $(\sigma_y \text{ and } \eta_p)$  of thermal greases. The solid points indicate the experimental data points obtained from Anton Paar parallel plate rheometer and the curves represent the Bingham plastic rheological model  $(\sigma = \sigma_y + \eta_p \dot{\gamma})$  curve fit.

### Characterization of the Thermal Conductivity of the Thermal Greases

The thermal conductivity of thermal greases is characterized using the transient hotwire (THW) methodology. The thermal grease is filled within a 12.3 mm diameter, 50 mm long test tube, through which a 25  $\mu$ m diameter tungsten wire passes. The thermal grease encapsulates the wire, such that the wire acts as a line heat source at the center (r=0) of the test tube (and the thermal grease). Current (0.1 A provided by a Keithley 2604B Source Meter) is passed through the tungsten wire, which acts as the heat source due to Joule heating. We measure the evolution of electrical resistance ( $R_{el}$ ) as a function of time using 4-wire measurements. We sample data every 1.67 ms for a heating period of 1 s and calculate the temperature rise of the wire as  $\Delta T = (R_{el}/R_{el,o} - 1)/\beta$ , where  $R_{el,o}$  is the electrical resistance at t=0 and  $\beta$  is the temperature coefficient of resistance. We calibrate  $\beta=0.00303$  1/K in our experiments by ensuring the thermal conductivity of de-ionized water

to be 0.614 W/(m K) in the same THW setup.<sup>35</sup> Finally, a linear fit for the slope ( $\zeta$ ) of the temperature rise as a function of log(t) (i.e.,  $\zeta = d(\Delta T)/d(log(t))$ ) enables estimation of the thermal conductivity as  $k = q'/(4\pi\zeta)$ , where  $q' = I^2R_{el,o}/L$  is the input heat source per unit length. Fig. 11 shows the transient temperature rise curves for all the thermal greases. We repeat the measurement three times for each thermal grease to consider variations within the experiment and report the average results in Table 1.

### Infrared Imaging of Thermal Grease

We leverage high-resolution IR imaging of thermal grease by using an infrared microscope (Quantum Focus Instruments (QFI) Corporation InfraScope<sup>TM</sup>) to capture 2D temperature maps and movies highlighting the degradation phenomenon. To obtain an accurate temperature map from an IR microscope, the emissivity of thermal greases must be quantified

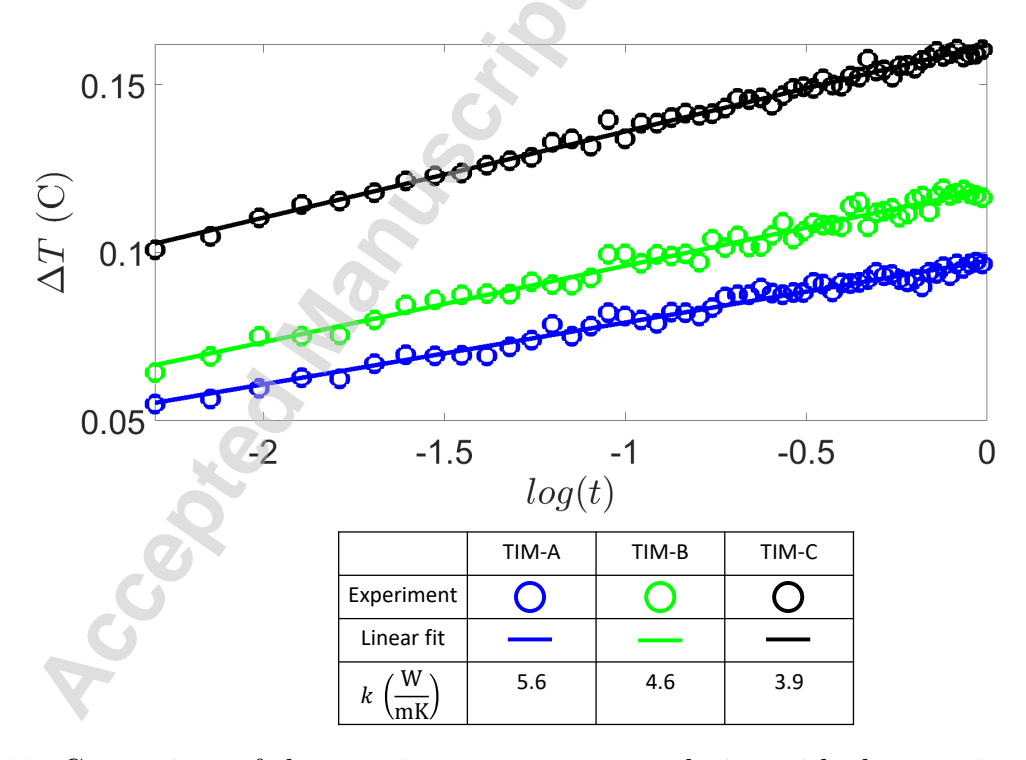


Figure 11: Comparison of the transient temperature evolution with the transient hot wire method for the three thermal greases. The slope of temperature rise curves with respect to log(t),  $\zeta = d(\Delta T)/d(log(t))$ , is inversely related to the thermal conductivity, while the offsets are related to other factors like contact resistances. Thus, TIM-A has the highest thermal conductivity with the shallowest slope.

apriori. Within the mechanical cycling experiments, the thermal grease constantly moves due to mechanical motion and voids are formed resulting in the difficulty of emissivity calibration in situ. Therefore we characterize the emissivity of thermal greases ex situ using a thermal stage at fixed temperatures. We first dispense the thermal grease on a thermal stage at very thin bond lines of 23  $\mu$ m and squeeze it with the same sapphire window used in mechanical cycling experiments (refer to the section on Mechanical cycling of thermal greases). Next, the thermal stage temperature is increased from 40 °C to 100 °C, and emissivity is measured at regular temperature intervals. Since the BLT at which thermal grease is dispensed is very thin and there is no active cooling of the sapphire window, we neglect any temperature gradient through the thermal grease thickness. At a fixed temperature, the radiation from the top surface of thermal grease is compared to the blackbody radiation expected at the same temperature, and the pixel-by-pixel emissivity is characterized. Next, we average the pixel-by-pixel emissivity through the entire thermal grease and use a constant value to calculate temperatures in the mechanical cycling experiments. As the temperature of the thermal stage is increased, the emissivity value converges to a single value highlighted in Table 2.

Table 2: Apparent emissivity of the thermal greases (based on the QFI InfraScope<sup>TM</sup> detector).

TIM	Emissivity	
TIM-A	$0.59 \pm 0.01$	
TIM-B	$0.57 \pm 0.01$	
TIM-C	$0.57 \pm 0.01$	

# References

(1) Lau, J. H. Overview and Outlook of Three-Dimensional Integrated Circuit Packaging, Three-Dimensional Si Integration, and Three-Dimensional Integrated Circuit Integration. *Journal of Electronic Packaging* 2014, 136, 040801.

- (2) Zhang, S.; Li, Z.; Zhou, H.; Li, R.; Wang, S.; Paik, K.-W.; He, P. Challenges and recent prospectives of 3D heterogeneous integration. e-Prime Advances in Electrical Engineering, Electronics and Energy 2022, 2, 100052.
- (3) Bird, H. M. Approaches to Electronic Miniaturization. *IEEE Transactions on Components Packaging and Manufacturing Technology Part A* **1995**, *18*, 274–278.
- (4) Henry, R. L.; Scal, R. K.; Shapiro, G. New Techniques for Electronic Miniaturization.

  Proceedings of the IRE 1950, 38, 1139–1145.
- (5) Iwai, H. (Gordon E. Moore Award) Impact of Micro-/Nano-Electronics, Miniaturization Limit, and Technology Development for the Next 10 Years and After. ECS Transactions 2021, 102, 81–95.
- (6) Mudawar, I. Recent advances in high-flux, two-phase thermal management. ASME 2013 Heat Transfer Summer Conf. Collocated with the ASME 2013 7th Int. Conf. on Energy Sustainability and the ASME 2013 11th Int. Conf. on Fuel Cell Science, Engineering and Technology, HT 2013. 2013.
- (7) Mudawar, I. Assessment of High-Heat-Flux Thermal Management Schemes; 2001; Vol. 24.
- (8) Ramakrishnan, B. et al. CPU Overclocking: A Performance Assessment of Air, Cold Plates, and Two-Phase Immersion Cooling. *IEEE Transactions on Components, Pack-aging and Manufacturing Technology* 2021, 11, 1703–1715.
- (9) Zhou, Y.; Wu, S.; Long, Y.; Zhu, P.; Wu, F.; Liu, F.; Murugadoss, V.; Winchester, W.; Nautiyal, A.; Wang, Z.; Guo, Z. Recent Advances in Thermal Interface Materials. 2020.
- (10) Prasher, R. S.; Shipley, J.; Prstic, S.; Koning, P.; Wang, J. L. Thermal resistance of particle laden polymeric thermal interface materials. *Journal of Heat Transfer* 2003, 125, 1170–1177.

- (11) Prasher, R. S.; Matayabas, J. C. Thermal contact resistance of cured gel polymeric thermal interface material. *IEEE Transactions on Components and Packaging Technologies* **2004**, *27*, 702–709.
- (12) Prasher, R. Thermal Interface Materials: Historical Perspective, Status, and Future Directions. *Proceedings of the IEEE* **2006**, *94*, 1571–1586.
- (13) Zhang, X. D.; Zhang, Z. T.; Wang, H. Z.; Cao, B. Y. Thermal Interface Materials with High Thermal Conductivity and Low Young's Modulus Using a Solid-Liquid Metal Codoping Strategy. ACS Applied Materials and Interfaces 2022, 15, 3534–3542.
- (14) Su, Y.; Ma, Q.; Liang, T.; Yao, Y.; Jiao, Z.; Han, M.; Pang, Y.; Ren, L.; Zeng, X.; Xu, J.; Sun, R. Optimization of Effective Thermal Conductivity of Thermal Interface Materials Based on the Genetic Algorithm-Driven Random Thermal Network Model. ACS Applied Materials and Interfaces 2021, 13, 45050–45058.
- (15) Uppal, A.; Kong, W.; Rana, A.; Wang, R. Y.; Rykaczewski, K. Enhancing Thermal Transport in Silicone Composites via Bridging Liquid Metal Fillers with Reactive Metal Co-Fillers and Matrix Viscosity Tuning. ACS Applied Materials and Interfaces 2021, 13, 43348–43355.
- (16) Jiang, H.; Wang, Z.; Geng, H.; Song, X.; Zeng, H.; Zhi, C. Highly Flexible and Self-Healable Thermal Interface Material Based on Boron Nitride Nanosheets and a Dual Cross-Linked Hydrogel. ACS Applied Materials and Interfaces 2017, 9, 10078–10084.
- (17) Marconnet, A. M.; Yamamoto, N.; Panzer, M. A.; Wardle, B. L.; Goodson, K. E. Thermal conduction in aligned carbon nanotube-polymer nanocomposites with high packing density. ACS Nano 2011, 5, 4818–4825.
- (18) Prasher, R. S. Surface Chemistry and Characteristics Based Model for the Thermal Contact Resistance of Fluidic Interstitial Thermal Interface Materials. *Journal of Heat* Transfer 2001, 123, 969–975.

- (19) Prasher, R. Rheology based modeling and design of particle laden polymeric thermal interface materials. *IEEE Transactions on Components and Packaging Technologies* **2005**, *28*, 230–237.
- (20) Prasher, R. S.; Koning, P.; Shipley, J.; Devpura, A. Dependence of Thermal Conductivity and Mechanical Rigidity of Particle-Laden Polymeric Thermal Interface Material on Particle Volume Fraction. *Journal of Electronic Packaging* 2003, 125, 386–391.
- (21) Nagrani, P. P.; Kulkarni, R. V.; Kelkar, P. U.; Corder, R. D.; Erk, K. A.; Marconnet, A. M.; Christov, I. C. Data-driven rheological characterization of stress buildup and relaxation in thermal greases. *Journal of Rheology* 2023, 67, 1129–1140.
- (22) Chiu, C. P.; Chandran, B.; Mello, M.; Kelley, K. An accelerated reliability test method to predict thermal grease pump-out in flip-chip applications. *Proceedings Electronic Components and Technology Conference* **2001**, 91–97.
- (23) Carlton, H.; Pense, D.; Huitink, D. Thermomechanical Degradation of Thermal Interface Materials: Accelerated Test Development and Reliability Analysis. *Journal of Electronic Packaging, Transactions of the ASME* **2020**, *142*.
- (24) Nnebe, I. M.; Feger, C. Drainage-induced dry-out of thermal greases. *IEEE Transactions on Advanced Packaging* **2008**, *31*, 512–518.
- (25) Due, J.; Robinson, A. J. Reliability of thermal interface materials: A review. Applied Thermal Engineering. 2013; pp 455–463.
- (26) Khuu, V.; Osterman, M.; Bar-Cohen, A.; Pecht, M. Effects of temperature cycling and elevated temperature/humidity on the thermal performance of thermal interface materials. *IEEE Transactions on Device and Materials Reliability* **2009**, *9*, 379–391.
- (27) D. DeVoto; J. Major; P. Paret; Institute of Electrical and Electronics Engineers Degradation Characterization of Thermal Interface Greases. 16th IEEE Intersociety Confer-

- ence on Thermal and Thermomechanical Phenomena in Electronic Systems (ITherm)
  2017,
- (28) Paisner, S. N.; Touzelbaev, M.; Refai-Ahmed, G.; Yang, Y. New developments for a nopump-out high-performance thermal grease. 2010 12th IEEE Intersociety Conference on Thermal and Thermomechanical Phenomena in Electronic Systems, ITherm 2010. 2010.
- (29) Nagrani, P. P.; Kulkarni, R. V.; Marconnet, A. M. Influence of Thermal Cycling on Degradation Behavior of Thermal Greases. 2023 22nd IEEE Intersociety Conference on Thermal and Thermomechanical Phenomena in Electronic Systems (ITherm). 2023; pp 01–10.
- (30) Kulkarni, R. V.; Nagrani, P. P.; Marconnet, A. M. In situ Optical Observations of Degradation of Thermal Greases with Thermal Cycling. 2023 22nd IEEE Intersociety Conference on Thermal and Thermomechanical Phenomena in Electronic Systems (ITherm). 2023; pp 1–8.
- (31) Nagrani, P. P.; Marconnet, A. M. Accelerated Testing of Thermal Grease Degradation: Combined Thermal Gradients and Forced Mechanical Cycling. 2024 23rd IEEE Intersociety Conference on Thermal and Thermomechanical Phenomena in Electronic Systems (ITherm). 2024; pp 1–8.
- (32) The Engineering ToolBox Metals, Metallic Elements and Alloys Thermal Conductivities. 2005; https://www.engineeringtoolbox.com/thermal-conductivity-metals-d\_858.html.
- (33) Narumanchi, S.; Mihalic, M.; Kelly, K.; Eesley, G. Thermal interface materials for power electronics applications. 2008 11th IEEE Intersociety Conference on Thermal and Thermomechanical Phenomena in Electronic Systems, I-THERM. 2008; pp 395– 404.

- (34) Kamani, K.; Donley, G. J.; Rogers, S. A. Unification of the Rheological Physics of Yield Stress Fluids. *Physical Review Letters* **2021**, *126*.
- (35) Mao, Y.; Robinson, J.; Binner, E. Understanding heat and mass transfer processes during microwave-assisted and conventional solvent extraction. *Chemical Engineering Science* **2021**, *233*.